IEEE Photonics Journal
An IEEE Photonics Society Publication

Open Access

A Feasibility Study of Broadband White Light Emitting Diode (WLED) Based Full-Field Optical Coherence Microscopy (FF-OCM) Using Derivative-Based Algorithm

Volume 9, Number 2, April 2017

Tulsi Anna
Ting-Wei Chang
Chih-Ming Lai
Arthur Chiou
Wen-Chuan Kuo

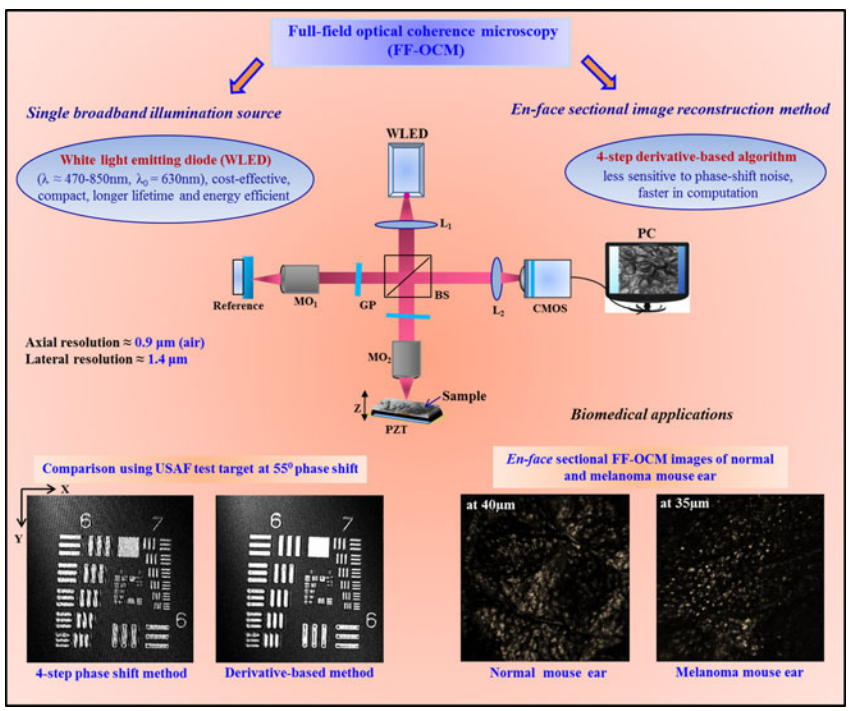

DOI: 10.1109/JPHOT.2017.2686978
1943-0655

A Feasibility Study of Broadband White Light Emitting Diode (WLED) Based Full-Field Optical Coherence Microscopy (FF-OCM) Using Derivative-Based Algorithm

Tulsi Anna,[1] Ting-Wei Chang,[2] Chih-Ming Lai,[3] Arthur Chiou,[4] and Wen-Chuan Kuo[4]

[1]Biophotonics and Molecular Imaging Research Center, National Yang-Ming University, Taipei 11221, Taiwan
[2]Biomedical Technology and Device Research Laboratories, Industrial Technology Research Institute, Hsinchu 31040, Taiwan
[3]Department of Electronic Engineering, Ming Chuan University, Taoyuan 111, Taiwan
[4]Institute of Biophotonics, Biophotonics and Molecular Imaging Research Center, National Yang-Ming University, Taipei 11221, Taiwan

DOI:10.1109/JPHOT.2017.2686978

Manuscript received December 22, 2016; revised March 10, 2017; accepted March 19, 2017. Date of publication March 24, 2017; date of current version April 11, 2017. This work was supported in part by the Ministry of Science and Technology, Taiwan: MOST 105-2112-M-010-002-MY3, and in part by the Biophotonics and Molecular Imaging Research Center, National Yang-Ming University, Taipei, Taiwan. Corresponding author: W.-C. Kuo (e-mail: wckuo@ym.edu.tw).

Abstract: Developing cost-effective and fast detection methods in full-field optical coherence microscopy (FF-OCM) platform for biological applications is of prime focus today. In this paper, we report a cost-effective Linnik type FF-OCM system with a single broadband white light emitting diode (WLED) (470–850 nm, $\lambda_0 = 630$ nm) light source in conjunction with a derivative-based image reconstruction algorithm. Sequential 2-D multiple phase-shifted interferograms were obtained by moving the sample stage using piezoelectric transducer and recorded *via* a 2-D charge complementary oxide semiconductor camera. Subsequently, the *en-face* sectional images were reconstructed using a derivative-based algorithm. The measured axial and lateral resolutions along with interferometric phase stability of the system were 0.9 μm, 1.4 μm, and 11 mrad, respectively. The advantages of the derivative-based algorithm over 4-step phase shifted method were demonstrated using USAF target and onion as test samples. Moreover, studies via the present system of the microstructure of skin epidermis in mouse ear with melanoma showed a significant deterioration from normal mouse skin in stratum corneum of the epidermis. This is the first study of the application of a derivative-based algorithm for biological samples in FF-OCM wherein WLED is used as a light source. The present system is stable, compact, and cost-effective compared to the conventional FF-OCM systems and provides comparable spatial resolution.

Index Terms: Full-field optical coherence microscopy (FF-OCM), imaging system, derivative-based algorithms, white light emitting diodes, melanoma.

1. Introduction

Optical coherence tomography (OCT), which is a non-invasive, micron scale cross-sectional depth resolved imaging technology, based on low coherence interferometry, has been developed for

several biomedical and engineering applications [1]. To achieve high axial resolution in conventional OCT, broadband light sources such as near infrared light emitting diodes (LEDs), superluminescent diodes (SLDs), Ti: sapphire laser and white light have been generally used. To realize high lateral resolution, high numerical aperture (NA$\geq$ 0.30) microscope objectives (MOs) have been used, and OCT is then referred as optical coherence microscopy (OCM) [2]. Along with axial and lateral resolutions, sensitivity, image acquisition speed, and the center wavelength of the light source are also important parameters which determine the performance of OCT/OCM systems. Additionally, faster OCT image reconstruction methods are also necessary for both *in vitro* and *in vivo* biological imaging. Thus, high-speed and high-sensitive frequency domain based OCT systems are of prime focus recently [3]. These systems use raster scanning to obtain 3-D images of biological samples. However, in full-field OCT/OCM (FF-OCT/FF-OCM), X-Y *en-face* sectional images with high lateral resolution can be obtained in a single exposure using 2-D charge coupled device (CCD) [4], [5] or charge complementary oxide semiconductor (CMOS) cameras [6], [7].

The *en-face* sectional imaging is useful to obtain temporal information within the *en-face* plane which is complementary to the longitudinal sectional imaging. Till date, various FF-OCT/FF-OCM systems based on both time and frequency domain techniques for the quantitative imaging of biological samples have been developed [4]–[17]. Most of these techniques have utilized broadband infrared SLDs and white light sources based on thermal, halogen and xenon arc lamps to achieve high axial resolution. Among these white light sources, high power halogen light sources have several advantages as they provide highest axial resolution in FF-OCM till date; for example, axial resolutions of 1.8 μm (center wavelength $\lambda_0 = 800$ nm, full width at half maxima (FWHM) $\Delta\lambda = 300$ nm) [14], 1 μm with quasi-monochromatic illumination ($\lambda_0 = 710$ nm, $\Delta\lambda = 10$ nm) [15], and 0.5 μm at $\lambda_0 = 700$ nm, have been reported [16].

In addition to these aforementioned light sources, over the past decade, LEDs, compact in design and cost-effective, have also been used widely as interferometric light sources for surface profilometry and microscopic imaging [17]–[21]. Compared to coherent light sources, LEDs have significant advantages due to their short temporal coherence and spatial incoherence which eliminate the background and speckle noises. Due to these advantages, LEDs have become the choice for digital holography (LED of $\lambda_0 = 630$ nm, $\Delta\lambda = 21$ nm), quantitative phase imaging [19], and white light interferometry (white light *LED* $\lambda_0 = 510$ nm, $\Delta\lambda = 35$ nm) for microstructure evaluation [20]; and a dual wavelength white LED has been used in vertical scanning interferometry [21]. Apart from these, infrared and combination of visible wavelength range (red, green, and blue) LEDs also have proven their impact in OCT techniques for different applications.

An infrared LED with $\lambda_0 = 840$ nm in FF-OCT with 1 μm axial resolution, higher compared to SLD based OCT systems, has been reported [5]. An FF-OCT with 3.6 μm axial resolution using an infrared LED ($\lambda_0 = 850$ nm, $\Delta\lambda = 90$ nm) has also been demonstrated for non-destructive testing of polymer coating on pharmaceutical pellets [22]. Besides, combinations of red, green, and blue (RGB) LEDs in FF-OCM have also been reported with a moderate axial resolution of 10 μm [23]. Further, a multi-wavelength RGB LED for skin imaging with a high axial resolution of $\approx$ 0.7 μm for red and $\approx$ 0.6 μm for both green and blue has been demonstrated [24], [25]. Apart from these LEDs, a single broadband white-light-emitting-diode (WLED) also has the great potential to be used in FF-OCM systems for *en-face* sectional imaging. WLEDs have their advantages of having large bandwidth, which can easily provide a high axial-resolution (on the order of submicron) in FF-OCM as compared to single-color and RGB LEDs. Recently, we have first reported the application of single broadband WLED of wavelength range 470-850 nm ($\lambda_0 = 630$ nm) in FF-OCM systems with an axial resolution of 0.9 μm [26], while Dubois *et al.* have compared the performance of WLED with halogen light sources [27]. Another related work is the use of a nitride-based white-light-emitting-diode (WLED) ($\lambda_0 = 532$ nm, $\Delta\lambda = 190$ nm) in a low coherence interferometric system to obtain the spectroscopic information with an axial resolution of 1 μm, [28]. WLED bears advantages over halogen based light sources due to its higher energy efficiency, longer lifetime, compactness, easy configuration with optics, less heat dissipation, as well as capability of providing high axial resolution in FF-OCM systems.

In addition to the light sources and parameters as mentioned above, fast and efficient *en-face* image reconstruction methods are also necessary in FF-OCT/FF-OCM for the biomedical imaging. In general, in FF-OCM systems, *en-face* sectional OCT images are reconstructed using 4 or 5 phase shifting algorithms *i.e.* from a series of images obtained at different phase steps [14]–[16], [27], [29], [30] using the concept of Hariharan algorithm [31]. Apart from this, in FF-OCM, a 4-integration buckets algorithm was also reported wherein four circularly phase shifted images were acquired to reconstruct an amplitude image [5]. Although the 4 or 5-step phase shifted image reconstruction algorithms are widely popular instead of 1 or 2 phase step methods where the background component in the raw interferogram can be removed *via* optics modification [32]–[34] or advanced image processing [35]–[37], phase shifting methods need to calculate the phase shift angle (*a priori* information is required) to modulate either the reference or sample signals which make the algorithm relatively slower in computation. Chang *et al*. [38] reported an efficient image reconstruction method based on discrete time differences corresponding to the depth sequences of interferometric signals known as "Derivative-based algorithm." To reconstruct the *en-face* sectional images using this algorithm, a concept from Energy Operator approach to calculate high-order derivatives of sequential images was exploited [39]. This method is suitable for multi-step phase shifted interferometric images without the requirement of phase shift angle calculation and hence is relatively faster in computation. Further, this method is less sensitive to phase shift noise when compared to traditional phase-shifting methods. Chang *et al*. successfully compared the derivative-based algorithm with existing multiple phase shifting methods via simulation and imaging of "alphabetic character" written on a solid reflecting substrate [38].Though the derivative-based method provides several advantages over existing approaches, till date, this method has not been well explored for FF-OCT/FF-OCM systems for the complex structure analysis of biological samples.

In this work, we report a cost-effective Linnik type FF-OCM system with single broadband WLED (470-850 nm, $\lambda_0 = 630$ nm) in conjunction with derivative-based amplitude demodulation algorithm. To the best of our knowledge, till date, this is the first study of the application of derivative-based image reconstruction algorithm in FF-OCM system for biological samples wherein a WLED is used as the light source. The 2-D spatial multiple phase shifted interferograms at different depths of the sample were obtained by moving the sample stage with a computer controlled piezoelectric transducer (PZT) and recorded using a 2-D CMOS camera. The detail performance and feasibility of the WLED in FF-OCM system using derivative-based algorithm were demonstrated by imaging highly scattering onion bulk sample and skin melanoma on mouse ear (and compared with that of the normal mouse). Our approach of using WLED along with derivative-based method in FF-OCM provides a faster and cost-effective platform for high spatial resolution *en-face* sectional imaging.

2. Experimental Details of FF-OCM and Derivative-Based Image Reconstruction Algorithm

Fig. 1 shows the schematic of the Linnik based FF-OCM system with WLED illumination. The light from WLED (MBB1L3, 470-850 nm, $\lambda_0 = 630$ nm, Thorlabs) was collimated by a collimation adapter (L1) (SM1P25-A, Thorlabs) and directed into the Linnik interferometer with two identical MOs *viz.* MO1 and MO2 (10x, NA = 0.3, air, Olympus). Two identical glass plates (GP), with precise angular alignment, were used to compensate for the dispersion mismatch and optimized axial resolution. The reference mirror was always kept in focus for different sample alignments using MO1 *via* a computer controlled translational stage. The sample stage was attached to a high-precision PZT (NF15AP1/M, Piezoelectric translational, 25 nm resolution, Thorlabs) to obtain multiple sequential phase shifted interferograms with constant steps. Back reflected light from the sample and reference mirrors interfered at the beam splitter (BS). The interferometric signal was projected on a CMOS camera (PointGrey, GS3-U3-23S6M, 1920 (H) x 1200 (V) pixels, pixel size 5.86 μm, ADC 12 bits, full well pixel capacity (FWC) 32,513 e^-, 163fps), by a lens L_2 (focal length = 60 mm).

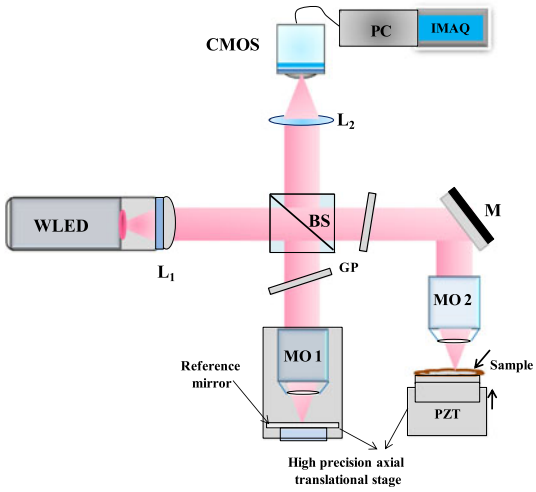

Fig. 1. Schematic of the FF-OCM set up using WLED.

The recorded spatial intensity distribution of interferometric signal, captured by CMOS camera while scanning axially through the sample, is usually written as [38]

$$I(x, y, t) = I_{DC}(x, y) + \gamma(x, y, t) A_i(x, y, t) \cos\left(\frac{2\pi}{\lambda_0} z(x, y, t) + \phi_s(x, y)\right) \tag{1}$$

where λ_0 is the center wavelength of the light source, $I_{DC}(x, y)$ is the background intensity corresponding to the direct component (DC) term, $\gamma(x,y,t)$ is the envelope of autocorrelation of the light source, $A_i(x, y, t)$ represents the amplitude of the *en-face* sectional OCT image, $z(x,y,t)$ the optical path difference between reference and sample arms, and $\phi_S(x, y)$ is the phase delay due to the sample. When the shift between two sequential images is very small compared to the coherence length of the light source, then $\gamma(x, y, t) \asymp 1$. In derivative-based algorithm multiple phase-shifted images are taken in a time sequence; subsequently, the first, second, and third derivatives of $I(x,y,t)$ with respect to the scanning time (t), namely, $I_1'(x, y, t)$, $I_1''(x, y, t)$, and $I_1'''(x, y, t)$, respectively, is expressed in terms of discrete differences of four sequential images of $I_1(x, y)$, $I_2(x, y)$, $I_3(x, y)$, $I_4(x, y)$ as [38]

$$I_1' = I_2(x, y) - I_1(x, y), \qquad I_1'' = I_3(x, y) - 2I_2(x, y) - I_1(x, y)$$
$$I_1''' = I_4(x, y) - 3I_3(x, y) + 3I_2(x, y) - I_1(x, y). \tag{2}$$

Combining these images represented by (2), the *en-face* sectional amplitude image at i^{th} layer can be obtained, without finding the phase shift angle [38]

$$A_i(x, y) = \Big|[(I_3(x, y) - 2I_2(x, y) - I_1(x, y)]^2 - \{I_4(x, y) - 3[I_3(x, y) - I_2(x, y)] - I_1(x, y)\}[I_2(x, y) - I_1(x, y)]\Big|^{1/2}. \tag{3}$$

The detail of the derivative-based algorithm and a comparison with phase shifting algorithm was explained through computational analysis in reference [38]. In the present work, all real-time image acquisition and image processing were done using LabView software.

3. Experimental Results and Discussion

A single broadband WLED based illumination was used to develop a FF-OCM system in conjunction with a derivative-based algorithm. In this section, the detailed characterization of the setup, as well as the performance and comparison of the system using derivative-based image reconstruction

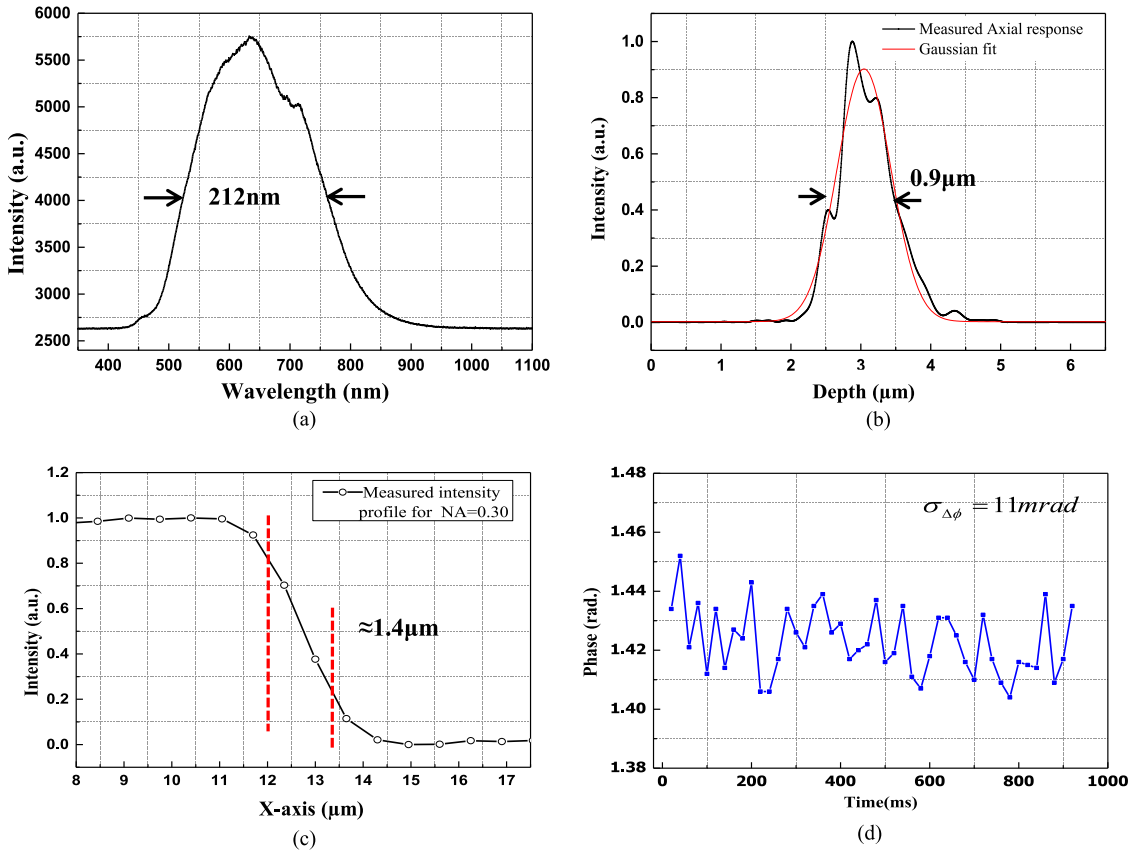

Fig. 2. (a) Measured spectrum of WLED source, (b) axial response, (c) the edge response of USAF 1951 resolution test-target, and (d) interferometric phase variations vs. time.

method with 4-step phase shifted method in imaging USAF 1951 test- target and onion bulk sample are discussed. Additionally, as a specific example of potential biomedical application, a microstructural study of the melanoma mouse skin epidermis is also discussed in comparison with normal mouse ear skin.

3.1 Characterization of WLED Based FF-OCM

3.1.1 Axial Resolution and Signal to Noise Ratio (SNR): The axial resolution of the FF-OCM system is governed by the coherence length of the light source and the refractive index of the medium [1]. Fig. 2(a) shows the measured spectrum of the light source using a spectrometer (Ocean Optics, USA) and the calculated FWHM ($\Delta\ \lambda$) was 212 nm.The calculated axial resolution of the present system was 0.82 μm, using $\Delta z = \frac{2\ln 2}{\pi n}(\frac{\lambda_0^2}{\Delta\lambda})$, $n =$ refractive index of air. The axial response was experimentally measured by using a plane reflecting mirror as a sample. The *en-face* sectional images were obtained by axially moving the sample mirror by PZT with 33 nm step size and a normalized intensity profile along the depth is shown in Fig. 2(b). The measured axial resolution at the surface of the sample was 0.9 μm, which is in good agreement with the calculated value. Having several advantages over existing thermal light sources such as halogen in FF-OCM, WLED, as our result shows, can provide comparable resolutions [16].

In addition to axial resolution, the signal to noise ratio (SNR) is also an important parameter. To measure the SNR of the present system, the experiment was performed by inserting an optical density filter (-1.3) in the sample arm with a round trip attenuation of 26 dB. A plane reflecting mirror was used as a test sample. An equal thickness of variable attenuator was used in the reference

arm to keep CMOS close to the saturation level to compensate for the optical path differences. Subsequently, the SNR was obtained from the axial response. The overall SNR of the system was determined to be -44 dB with 18 dB dynamic range without any averaging or summing of the interferograms at the same depth. Theoretically, in shot-noise limited case, it is calculated as 20 log ($N_e/\sqrt{N_e}$) [36], where N_e is the total number of electrons. Therefore using the full well capacity (FWC) of 32,513 e^-, the SNR can be obtained as $\approx$ 45 dB which is close to the experimentally obtained value. SNR is limited by the FWC of the camera as well as the illumination power of the light source [5]. Moreover, it is to be noted here that the camera in the present system could not be utilized for the highest frame rate corresponding to minimal exposure time as the WLED power is too low to saturate it. Therefore, in this study, the optimized CMOS frame rate of 50 fps at 10 ms exposure time was used to have the highest frame rate when the full power of WLED was utilized. In case a CMOS camera with high FWC were used, the SNR of the present FF-OCM using WLED would have been greatly improved.

3.1.2 Lateral Resolution: The lateral resolution (Δx) is defined as the FWHM of the point spread function (PSF) in a conventional diffraction-limited optical system and is calculated using $\Delta x = (0.61\,\lambda_0/NA)$ [5]. The calculated value of the lateral resolution of our system for 10x MO (NA = 0.3) was 1.28 μm. To measure it experimentally, a standard USAF 1951 test-target was imaged and the intensity profile across the lines of group 7 was plotted. Fig. 2(c) shows edge response and the 20 to 80% width of the intensity profile was obtained to be 1.4 μm, close to the calculated value. The edge response is the convolution of a perfect edge with the PSF. The measured imaging area of the sample was 755 x 755 μm^2 corresponding to 704 x 704 pixels on the camera.

3.1.3 Interferometric Phase Stability: We further measured the interferometric phase stability of the present system. Fig. 2(d) shows the phase variation at the surface of the sample mirror with respect to time. In this experiment, fifty consecutive spatial interferograms at fixed exposure time (with 50 fps) near CMOS saturation were acquired, and the phase images were evaluated. Assuming a uniform illumination of WLED, we selected 1 x 1 central pixels to evaluate the standard deviation $\sigma_{\Delta\varphi}$ of the measured phase and obtained to be 11 mrad (Fig. 2(d)). The phase stability, expressed in terms of standard optical path length (OPL) sensitivity as,$\sigma_{OPL} = (\lambda_0/4\pi n).\sigma_{\Delta\varphi}$ [40], was 0.6 nm at the sample surface, which is comparable to that of the SLD based FF-OCT systems [40]. Hence, the present system using WLED as the light source is also suitable for quantitative phase measurements in biological samples simultaneous with intensity based information.

3.2 Performance of Derivative-Based Algorithm

In the derivative-based algorithm, as mentioned previously in Sections 1 and 2, *en-face* sectional images were reconstructed using the high-order derivatives. It works with sequential multi-step phase shifted interferograms when the phase difference between two sequential images is as small as possible. Thus the *en-face* sectional image quality response should be evaluated for different phase shift increments. To validate the performance of the derivative-based algorithm, we used a USAF 1951 test-target as the sample. The sequential phase shifted interferograms of the USAF sample were acquired by moving the sample stage using PZT with a constant step following the procedure mentioned in Section 2. Since the PZT resolution of our system is 25 nm, therefore the minimum possible phase shift angle is $\approx$14°. In this measurement, a set of sequential interferograms were recorded corresponding to a set of phase shift angle increments, ranging from 18° to 90°. The *en-face* sectional images were then reconstructed using (3). Fig. 3(a) shows the relative intensity variance of *en-face* images for each phase shift increments with the input image. The intensity variances for all the *en-face* images at different phase shifts as well as the input image were calculated after normalizing the maximum gray value.

It can be seen from Fig. 3(a), that the relative intensity variance increases linearly with the phase shift increments. Hence, it can be inferred that the smaller phase shift angle ($< 90°$) would be better to calculate the *en-face* images using the derivative-based algorithm.

Further, the performance of the derivative-based method was compared with traditional 4-step phase shift image reconstruction method [31] using USAF 1951 test-target. Fig. 3(b) shows the

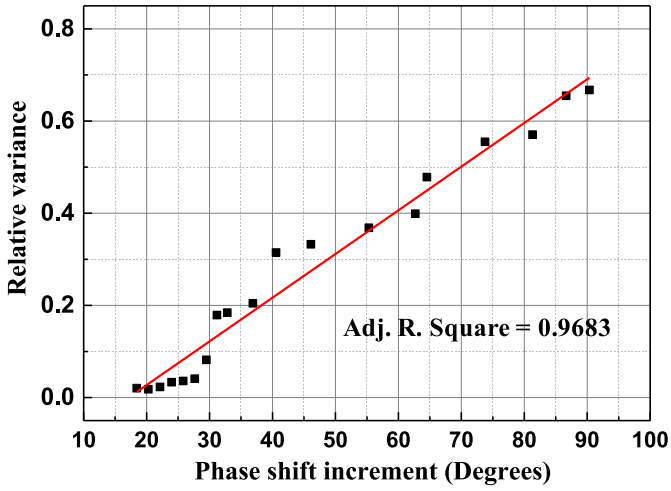

(a)

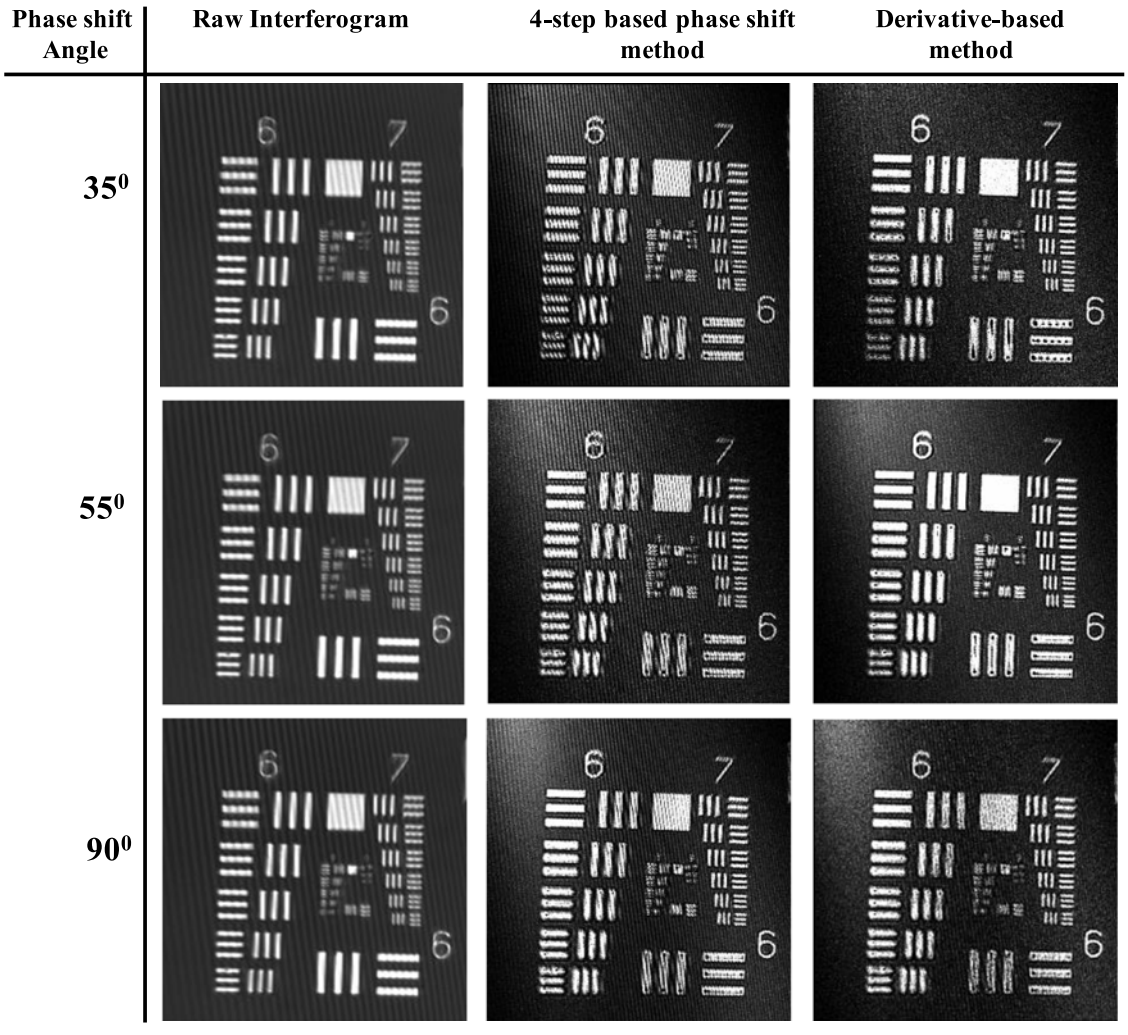

(b)

Fig. 3. (a) *En-face* sectional image quality response with phase shift increment and (b) a comparison of derivative-based method with 4-step based phase shift method using USAF 1951 test-target.

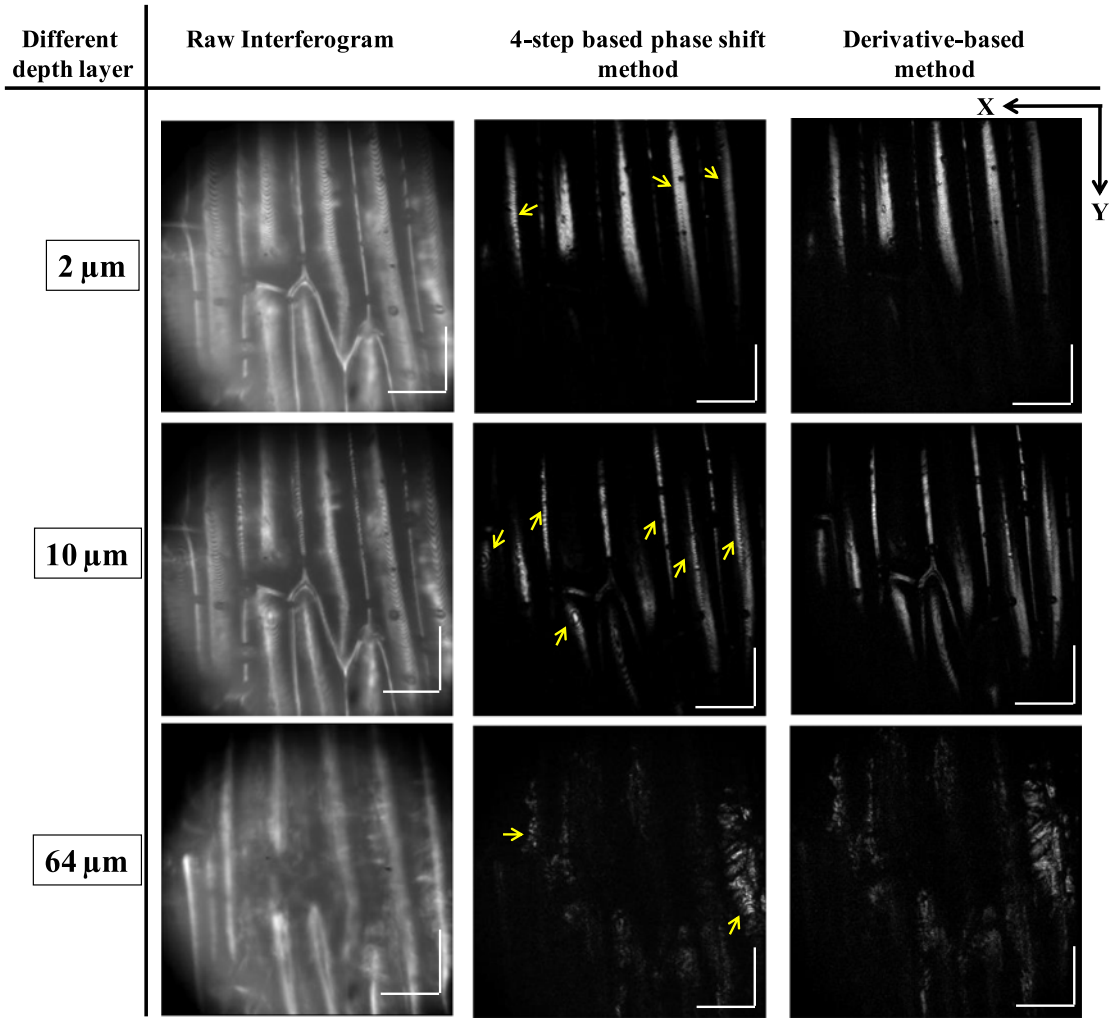

Fig. 4. Comparison of derivative-based method with 4-step based phase shift method using onion as test biological sample at different depths. Scale bar: 100 μm.

recorded raw interferograms of USAF 1951 test-target at phase shift angles 35°, 55°, and 90° and their corresponding reconstructed *en-face* images using 4-step based phase shift and derivative-based methods. From these images, it can be clearly seen that there are fewer interference fringes visible while using derivative-based method for each phase shift angle. Thus, it can be concluded that the performance of a derivative-based method for each phase shift angle is better than 4-step based phase shift method because it is less sensitive to the phase noise. Residual interference fringes in the reconstructed *en-face* images via 4-step based phase shift methods can be attributed to the high sensitivity of this method to phase changes.

To demonstrate the feasibility of our FF-OCM using derivative-based method for biological systems, onion bulk sample was considered. Furthermore, *en-face* image quality obtained *via* derivative-based was also compared with 4-step phase shift method. The power at the sample plane and the exposure time were 60 μW and 10 ms, respectively. The multiple phase-shifted interferograms were measured by moving the sample stage using PZT with a constant step of 33 nm ($\approx$18°) and the *en-face* images at different depths were reconstructed using both the derivative as well as 4-phase step methods. The phase shift angle was chosen at the lowest minimum possible in our system to minimize the probability of phase error occurrence from the irregular structural pattern of the biological sample. Fig. 4 shows the raw interferograms and corresponding e*n-face*

sectional images of onion bulk sample at 2, 10, and 64 μm depths, reconstructed using 4-step based phase shift and derivative-based methods. Visible residual interference fringes (as indicated by arrows) can be seen in the *en-face* sectional images at different depths for 4-step phase shift method while less visible fringes are observed in derivative-based method [see Fig. 4]. Hence, the performance of the derivative-based method is also better than 4-step phase shift method while imaging the biological sample. Further, it should be noted that the different cell organizations, such as cell wall, surface, as well as layers of the onion skin are clearly resolved in these sectional images [see Fig. 4].

3.3. Elucidating the Microstructural Changes in Melanoma Mouse Ear Skin Using Present FF-OCM

The feasibility of the present FF-OCM system with derivative-based image reconstruction method for potential biomedical applications was also demonstrated by elucidating the microstructural features of the skin of a melanoma mouse ear. The mouse ear skin provides an advantageous milieu to study diseases related to skin disorders [41]. Skin melanoma is a kind of cancer which develops from pigmented cells like melanocytes. Even though only 1% of all skin cancers are associated with melanoma, it accounts for most of the skin cancer deaths.

In this study, melanoma was induced topically in the ears of the C57BL/6J mouse (ten weeks old, female) and experiments were performed after five weeks of inducing melanoma *ex-vivo*. The FF-OCM images of the ear skin of both melanoma and normal mouse were recorded and compared. Fig. 5 shows the *en-face* sectional as well as stacked images of the skin of normal and melanoma mouse left ears.

The images were obtained using a 10x microscope objective (NA 0.3) for wide-area imaging. Fig. 5(a)–(c), shows the *en-face* sectional images of the normal mouse ear skin at depths 7, 15, and 40 μm, encompassing the stratum corneum (cornified layer), the uppermost layer of the epidermis of the skin and some inner parts of the epidermis layer. Further, epidermis layer of the melanoma mouse ear skin is shown in Fig. 5(d)–(f) at depths 10, 18, and 35 μm. Stratum corneum is formed of anucleated cells called corneocytes [42]. The cytoplasms of these cells are filled with a filamentous birefringent scleroprotein keratin [42]. From the images, regular polygonal shapes (as indicated by arrows) are observed in Fig. 5(a)–(c). However, such structures are not observed in melanoma mouse ear skins (see Fig. 5(e) and (f)); though some regular structures are observed at 10 μm in Fig. 5(d). The bright granular spots in each figure may be attributed to the scleroprotein keratin. Fig. 5(g) and (h) show the 3D stacked volume images of the normal and melanoma mouse ears, respectively, up to a depth of 50 μm; although deeper layers have been successfully imaged in our experiments, they reveal little distinguishable features. From these stacked images it can also be easily discernable that there is a distinct microstructural change at the stratum corneum of the skin epidermis.

Though images obtained through 10x microscope objective lens show distinguishable structural features, in this study, we have further used a 20x microscope objective lens with NA 0.4 (Newport, USA) to elucidate more microstructural features of epidermis layer. The murine epidermis layer has regular patterned microstructure [43]. Fig. 6(a)–(c) shows the epidermis layer at depths of 7, 15, and 30 μm of the normal mouse ear. Regular hexagonal microstructures, as indicated by dotted hexagons in Fig. 6(a)–(c) are clearly seen in the normal mouse ear. Cornified cells are usually hexagonal in shape and form the upper layer of the clonal epidermal proliferative unit (EPU) [43]. EPU forms the basis of the ordered architecture of epidermis. Additionally, dense fibrillar aggregates inside the cornified cells can also be seen in the *en-face* sectional images of the normal mouse ear skins [see Fig. 6(a)–(c)]. Our results further showed the absence of regular hexagonal microstructure of stratum corneum of the epidermis layer of the melanoma mouse ear skin [see Fig. 6 (d)–(f)]. Moreover, the fibrous aggregates of the stratum corneum were lost as indicated by hexagonal boxes in Fig. 6(d)–(f). Cornified cells are hence disintegrated, or the development of these cells is affected in the stratum corneum of the melanoma mouse ear.

Stratum corneum is the initial protection layer of the underlying tissues from pathogenic invasion, dehydration, chemicals etc. This layer also attributes the stretchy property of the skin. The formation

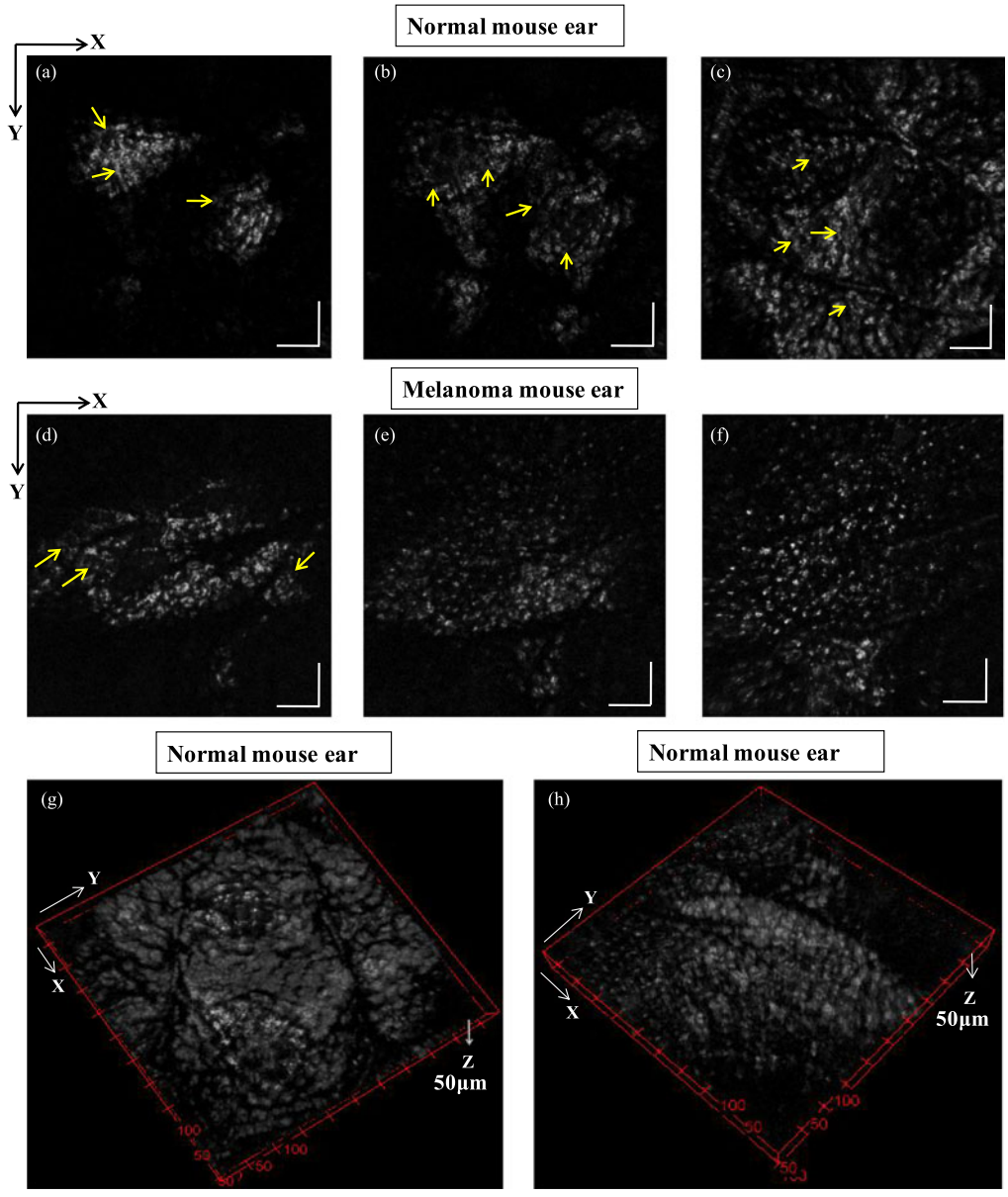

Fig. 5. E*n-face* sectional images of normal mouse ear [(a) – (c)] at 7, 15 and 40 μm and melanoma mouse ear [(d) – (f)] at 10, 18 and 35 μm depths, respectively. (g) and (h) stacked 3-D volume image of 500 x 500 x 90 μm^3 normal and melanoma mouse ears, respectively. Scale bar: 100 μm (10x, NA = 0.3).

of the cornified envelope is an important process in skin homeostasis and failure of which may lead to many skin disorders [44]. Wachsman *et al.* showed that RNA from the stratum corneum lesions provides sufficient information about the diagnosis of melanoma [45]. This may be due to the pagetoid cells (underlying cells of melanoma) extrusion to the stratum corneum [45]. Our FF-OCM *en-face* sectional images also show distinct architectural differences in the stratum corneum layers of the skin between normal and melanoma mouse ear skins. This result can serve as complementary information in the diagnosis of the melanoma development.

All the results presented above mentioned clearly show the applicability of the derivative-based algorithm in WLED based FF-OCM system for *en-face* sectional imaging of biological samples. In this work, we have compared the derivative-based algorithm with standard 4-step phase-shifted

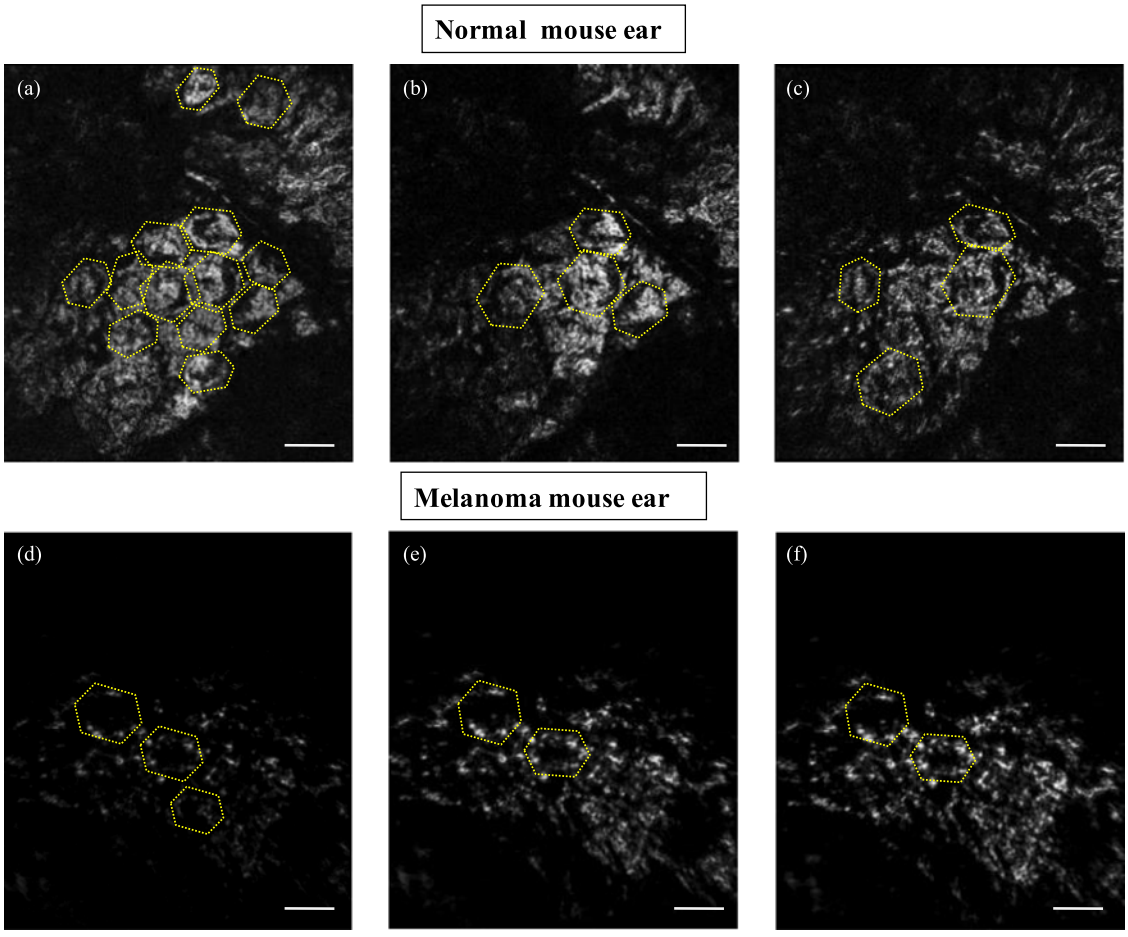

Fig. 6. E*n-face* sectional images of normal mouse ear [(a) – (c)] at 7, 15 and 30 μm and melanoma mouse ear [(d) – (f)] at 10, 18 and 22 μm depths, respectively. Scale bar: 50 μm (20x, NA = 0.4).

method. Though 4-step derivative-based method can provide FF-OCM images with minimal residual fringes when the phase shift angle is below 90° [38], in imaging biological samples, the residual fringes must be removed completely to extract all information from the FF-OCM images. Therefore, in the present study, the 4-step derivative-based method was used in conjunction with temporal (number of frame averaged n = 3) and spatial averaging (3 x 3 pixels) of the reconstructed FF-OCM images of biological samples. Another notable advantage of the derivative-based algorithm is that it does not need any apriori information of phase shift angle, which is needed in 4-step phase shifted method. We have compared the derivative-based algorithm with 4-step phase shifted method only; because the corresponding comparisons with lower order (one- or two-steps) methods are redundant as discussed in the introduction. Although higher order methods may provide better results compared with 4 step methods, it is necessary to use minimum best order method (viz. 4 step methods) to obtain better FF-OCM images of the biological samples, where the recording of more stacks of images are often needed (leading to longer time). Along with longer exposure time required in WLED illumination, and large number of images, the net image acquisition time may be significantly longer which may eventually damage the biological samples. These factors can limit the practicality of real-time imaging using FF-OCM. Moreover, the FF-OCM images are obtained by moving the sample stage *via* PZT which inherently generates higher background noise at higher depths while using high magnification such as 10x and 20x microscope objectives. Thus, derivative-based method, which automatically removes the DC noise, is suitable for obtaining highly resolved FF-OCM images. Our present approach of using derivative-based algorithm is faster in

computation, with low phase errors, and cost-effective compared to current state of art [13]–[16]. Further, the stability of the present system using WLED is high enough to achieve the quantitative phase measurements in biological samples simultaneously with intensity based information. This system offers a higher spatial resolution than the conventional SLDs and a fiber-optic based OCT systems; the spatial resolution achieved is comparable with those equipped with halogen light source. Although the system performance is limited due to moderate penetration depth caused by the highly scattering properties of the biological samples in the visible range of the light source, it is sufficient to provide in-depth structural information of onion bulk and mouse ear skin images (see Figs. 4–6).

4. Conclusion

To summarize, we have successfully demonstrated a cost-effective high-resolution FF-OCM system based on the Linnik-type microscope using a single broadband WLED (470-850 nm) and 2-D CMOS camera with the derivative-based method for *en-face* image reconstruction. Experimentally achieved axial and lateral resolutions were 0.9 and 1.4 μm, respectively with measured sensitivity $\approx$ -44 dB (limited by FWC of CMOS). The interferometric phase stability was determined to be 11 mrad. The derivative-based method is successfully utilized for the first time while using WLED illumination in the FF-OCM system for reconstruction of the sequential *en-face* sectional images of biological samples. The microstructures of the ear skins of normal mouse and melanoma induced mouse were also compared using our approach. Our results showed a significant microstructural change of the stratum corneum of the melanoma mouse ear skin when compared with the normal mouse. These results can serve to complement other existing methods in the diagnosis of melanoma. Our approach of using derivative-based algorithm is relatively faster in computation compared to 4-phase step algorithms and robust even when the phase shift angle is not so stable, provided that the phase shift between two sequential images is small enough to avoid high phase error. The present system is stable, compact, and cost-effective compared to the conventional FF-OCM systems and provides comparable spatial resolution. It is expected that using a high power WLED, in conjunction with a highly sensitive detection unit, and proper reconstruction methods, this system would be useful for studying complex biological structures.

References

[1] W. Drexler and J. G. Fujimoto, *Optical Coherence Tomography, Technology and Applications*, New York, NY, USA: Springer, 2008.
[2] J. A. Izatt, M. D. Kulkarni, H. W. Wang, K. Kobayashi, and M. V. Sivak, "Optical coherence tomography and microscopy in gastrointenstinal tissues," *IEEE J. Sel. Topics Quantum Electron.* vol. 2, no. 4, pp. 1017–1028, Dec. 1996.
[3] M. Wojtkowski, "High-speed optical coherence tomography: basics and applications," *Appl. Opt.*, vol. 49, no. 16, pp. D30–D61, Jun. 2010.
[4] E. Beaurepaire, A. C. Boccara, M. Lebec, L. Blanchot, and H. Saint-Jalmes, "Full-field optical coherence microscopy," *Opt. Lett.*, vol. 23, no. 4, pp. 244–246, Feb. 1998.
[5] A. Dubois, L. Vabre, A. C. Boccara, and E. Beaurepaire, "High-resolution full-field optical coherence tomography with a Linnik microscope," *Appl. Opt.* vol. 41, no. 4, pp. 805–812, Feb. 2002.
[6] P. Egan, F. Lakestani, and M. J. Connelly, "Full-field optical coherence tomography with a complimentary metal-oxide semiconductor digital signal processor camera," *Opt. Eng.*, vol. 45, no. 1, pp. 015601–015607, Jan. 2006.
[7] Y. Watanabe and M. Sato, "Three-dimensional wide-field optical coherence tomography using an ultrahigh-speed CMOS camera," *Opt. Commun.*, vol. 281, no. 7, pp. 1889–1895, Apr. 2008.
[8] W. Y. Oh, B. E. Bouma, N. Iftimia, R. Yelin, and G. J. Tearney, "Spectrally-modulated full-field optical coherence microscopy for ultrahigh-resolution endoscopic imaging," *Opt. Exp.*, vol. 14, no. 19, pp. 8675–8684, Sep. 2006.
[9] A. Dubois, J. Moreau, and C. Boccara, "Spectroscopic ultrahigh- resolution full-field optical coherence microscopy," *Opt. Exp.*, vol. 16, no. 21, pp. 17082–17091, Oct. 2008.
[10] T. Anna, V. Srivastava, D. S. Mehta, and C. Shakher, "High-resolution full-field optical coherence microscopy using a Mirau interferometer for the quantitative imaging of biological cells," *Appl. Opt.*, vol. 50, no. 34, pp. 6343–6351, Dec. 2011.
[11] V. Srivastava, S. Nandy, and D. S. Mehta, "High-resolution corneal topography and tomography of fish eye using wide-field white light interference microscopy," *Appl. Phy. Lett.* vol. 102, no. 15, pp. 153701–153704, Apr. 2013.
[12] B. Huang, P. Bu, X. Wang, N. Nan, and X. Guo, "Full-range parallel Fourier-domain optical coherence tomography using a spatial carrier frequency," *Appl. Opt.* vol. 52, no. 5, pp. 958–965, Feb. 2013.

[13] O. Assayag *et al.*, "Imaging of non-tumorous and tumorous human brain tissues with full-field optical coherence tomography," *NeuroImage Clin.*, vol. 2, pp. 549–557, Apr. 2013.
[14] A. Dubois, K. Grieve, G. Moneron, R. Lecaque, L. Vabre, and C. Boccara, "Ultrahigh-resolution full-field optical coherence tomography," *Appl. Opt.*, vol. 43, no. 14, pp. 2874–2883, May 2004.
[15] A. Safrani and I. Abdulhalim, "Ultrahigh-resolution full-field optical coherence tomography using spatial coherence gating and quasi-monochromatic illumination, *Opt. Lett.*, vol. 37, no. 4, pp. 458–460, Feb. 2012.
[16] A. Federici and A. Dubois, "Full-field optical coherence microscopy with optimized ultrahigh spatial resolution," *Opt. Lett.* vol. 40, no. 22, pp. 5347–5350, Nov. 2015.
[17] S. Dilhaire, S. Grauby, S. Jorez, L. D. P. Lopez, J. Rampnoux, and W. Claeys, "Surface displacement imaging by interferometry with a light emitting diode," *Appl. Opt.* vol. 41, no. 24, pp. 4996–5001, Aug. 2002.
[18] N. Warnasooriya and M. K. Kim, "LED-based multiwavelength phase imaging interference microscopy," *Opt. Exp.*, vol. 15, no. 15, pp. 9239–9247, Jul. 2007.
[19] R. Guo *et al.*, "LED-based digital holographic microscopy with slightly off-axis interferometry," *J. Opt.*, vol. 16, no. 12, pp. 125408–125415, Dec. 2014.
[20] I. Shavrin, L. Lipiäinen, K. Kokkonen, S. Novotny, M. Kaivola, and H. Ludvigsen, "Stroboscopic white-light interferometry of vibrating microstructures," *Opt. Exp.*, vol. 21, no. 14, pp. 16901–16907, Jul. 2013.
[21] W. K. Chong, X. Li, and Y. C. Soh, "Harnessing spectral property of dual wavelength white LED to improve vertical scanning interferometry," *Appl. Opt.*, vol. 52, no. 19, pp. 4652–4662, Jul. 2013.
[22] C. Li, J. A. Zeitler, Y. Dong, and Y.-C. Shen, "Non-destructive evaluation of polymer coating structures on pharmaceutical pellets using full-field optical coherence tomography," *J. Pharmaceutical Sci.*, vol. 103, no. 1, pp. 161–166, Jan. 2014.
[23] L. F. Yu and M. K. Kim, "Full-color three-dimensional microscopy by wide-field optical coherence tomography," *Opt. Exp.*, vol. 12, no. 26, pp. 6632–6641, Dec. 2004.
[24] B. W. Yang and X. C. Chen, "Full-color skin imaging using RGB LED and floating lens in optical coherence tomography," *Biomed. Opt. Exp.*, vol. 1, no. 5, pp. 1341–1346, Dec. 2010.
[25] B. W. Yang, Y. Y. Wang, Y. M. Lin, Y. S. Juan, H. T. Chen, and S. P. Ying, "Applying RGB LED in full-field optical coherence tomography for real-time full-color tissue imaging," *Appl. Opt.*, vol. 53, no. 22, pp. E56–E60, Aug. 2014.
[26] T. Anna, T. W. Chang, C. M. Lai, and W. C. Kuo, "White light diode (WLED) based high-resolution full-field optical coherence microscopy (FF-OCM)," pp 209, Focus on Micrsocopy FOM 2016, National Taiwan Univ. Hospital (NTHU), Taipei, Taiwan, http://www.focusonmicroscopy.org, Mar. 20-23, 2016.
[27] J. Ogien and A. Dubois, "High-resolution full-field optical coherence microscopy using a broadband light-emitting diode," *Opt. Exp.*, vol. 24, no. 9, pp. 9922–9931, May 2016.
[28] H. C. Cheng and C. K. Sun, "WLED-based low coherence interferometry in the visible wavelength range," *J. Med. Biol. Eng.*, vol. 27, no. 4, pp. 173–176, Dec. 2007.
[29] K. Grieve *et al.*, "*In vivo* anterior segment imaging in the rat eye with high speed white light full-field optical coherence tomography," *Opt. Exp.*, vol. 13, no. 16, pp. 6286–6295, Aug. 2005.
[30] S. Chang, X. Liu, X Cai, and C. P. Grover, "Full-field optical coherence tomography and its application to multiple-layer 2-D information retrieving," *Opt. Commun.*, vol. 246, no. 4/6, pp. 579–585, Feb. 2005.
[31] P. Hariharan, B. F. Orebam, and T. Eiju, "Digital phase-interferometry: A simple error-compensating phase calculation algorithm," *Appl. Opt.*, vol. 26, no. 13, pp. 2504–2506, Jul. 1987.
[32] C. Dunsby, Y. Gu, and P. M. W. French, "Single-shot phase-stepped wide-field coherence-gated imaging," *Opt. Exp.*, vol. 11, no. 2, pp. 105–115, Jan. 2003.
[33] M. Akiba, K. P. Chan, and N. Tanno, "Full-field optical coherence tomography by two-dimensional heterodyne detection with a pair of CCD cameras," *Opt. Lett.*, vol. 28, no. 10, pp. 816–818, May 2003.
[34] M. S. Hrebesh, R. Dabu, and M. Sato, "In vivo imaging of dynamic biological specimen by real-time single-shot full-field optical coherence tomography," *Opt. Commun.*, vol. 282 no. 4, pp. 674–683, Feb. 2009.
[35] M. S. Hrebesh and M. Sato, "Real-time single-shot full-field OCT based on dual-channel phase-stepper optics and 2-D quaternionic analytic signal processing," in *Proc. SPIE, Bio. Opt.*, 2009, Art. no. 71681H.
[36] T. Anna, D. S. Mehta, and M. Sato, "Improvement of the dynamic range using background subtraction in single shot wide-field optical coherence tomography," *Jr. Mod. Opt.*, vol. 62, no. 21, pp. 1816–1827, Jan. 2015.
[37] S. E. Schausberger, H. Bettina, S. Bernstein, and D. Stifter, "Full-field optical coherence microscopy with Riesz transform-based demodulation for dynamic imaging," *Opt. Lett.*, vol. 37, no. 23, pp. 4937–4939, Dec. 2012.
[38] S. Chang, X. Cai, and C. Fluerau, "An efficient algorithm used for full-field optical coherence tomography," *Opt. Lasers Eng.*, vol. 45, no. 12, pp. 1170–1176, Dec. 2007.
[39] B. Santhanam and P. Maragos, "Energy demodulation of two-component AM-FM signal mixtures," *IEEE Signal Process Lett.*, vol. 3, no. 11, pp. 294–298, Nov. 1996.
[40] T. Anna, S. Kimura, D. S. Mehta, and M. Sato, "Reflection, phase and en-face sectional imaging of scattering objects using quasi-single-shot wide-field optical coherence Tomography," *Opt. Rev.*, vol. 22, no. 5, pp. 706–716, Jul. 2015.
[41] J. C. Becker, R. Houben, D. Schrama, H. Voigt, S. Ugurel, and R. A. Reisfeld, "Mouse models for melanoma: a personal perspective," *Exp. Dermatol.*, vol. 19, no. 2, pp. 157–164, Feb. 2009.
[42] K. Gopinathan, G. Menona, W. Cleary, and E. L. Majella, "The structure and function of the stratum corneum," *Int. J. Pharmaceutics*, vol. 435, no. 1, pp. 3–9, Oct. 2012.
[43] D. P. Doupe´, A. M. Klein, B. D. Simons, and P. H. Jones, "The ordered architecture of murine ear epidermis is maintained by progenitor cells with random fate," *Develop. Cell*, vol. 18, no. 2, pp. 317–323, Feb. 2010.
[44] C. Blanpain and E. Fuchs, "Epidermal homeostasis: a balancing act of stem cells in the skin," *Nat. Rev. Mol. Cell Biol.*, vol. 10, no. 3, pp. 207–217, Mar. 2009.
[45] W. Wachsman, V. Morhenn, and T. Palmer, "Noninvasive genomic detection of melanoma," *Br. J. Dermatol.*, vol. 164, no. 4, pp. 797–806, Apr. 2011.